



Structural Parameters of the Thin Disk Population from Evolved Stars in the Solar Neighborhood

Sedanur İyisan¹, Selçuk Bilir², Özgecan Önal Taş², and Olcay Plevne²

¹ Istanbul University, Institute of Graduate Studies in Science, Programme of Astronomy and Space Sciences, 34116, Istanbul, Turkey

² Istanbul University, Faculty of Science, Department of Astronomy and Space Sciences, 34119, Istanbul, Turkey; sbilir@istanbul.edu.tr

Received 2024 November 15; revised 2025 January 6; accepted 2025 January 6; published 2025 February 12

Abstract

This study investigates the structural parameters of the thin-disk population by analyzing the spatial distribution of evolved stars in the solar neighborhood. From the Gaia Data Release 3 database, about 39.1 million stars within 1 kpc and with relative parallax errors $\sigma_{\varpi}/\varpi \leq 0.10$ were selected. The photometric data was corrected for extinction using a Galactic dust map. The sample was refined by considering the color–magnitude region $M_G \times (G_{BP} - G_{RP})_0$ associated with evolved stars, applying a stricter parallax error limit of $\sigma_{\varpi}/\varpi \leq 0.02$, and yielding 671,600 stars. The star sample was divided into 36 regions based on their Galactic coordinates, with evolved stars in the absolute magnitude range of $-1 < M_G \text{ (mag)} \leq 4$ further split into five one-unit magnitude intervals. This led to 180 subgroups whose space-density profiles were modeled using a single-component Galaxy model. The analysis shows that the space densities are in agreement with the literature and that the scale heights vary with $200 < H \text{ (pc)} < 600$ interval to their absolute magnitudes. Red clump stars in the solar neighborhood were also estimated to have a scale height of 295 ± 10 pc. These findings indicate that evolved stars with bright absolute magnitudes originate from the evolution of the early spectral-type stars with short scale height, while fainter ones come from the evolution of the intermediate spectral-type stars with large scale height, suggesting that variations in scale height reflect the contribution of Galactic evolution processes.

Unified Astronomy Thesaurus concepts: Milky Way disk (1050); Galaxy structure (622); Solar neighborhood (1509)

1. Introduction

Studies of the Galactic structure have been essential in advancing our understanding of the universe. Detailed analysis of the Milky Way allows us to address key astrophysical questions because we can observe it more closely than any other galaxy. Techniques such as star counting, alongside methods incorporating stellar chemistry, age, and kinematics, have been particularly useful for determining the Galaxy's structure (H. V. Peiris 2000). In particular, the star counting method helps constrain the Galaxy's components, assuming a density distribution similar to galaxies of the same Hubble type. According to the standard model, the Milky Way is a Hubble-type Sbc galaxy with an exponential disk and a spheroidal component (J. Binney & M. Merrifield 1998).

Since the 1980s, substantial progress has been made in Galactic structure research, particularly through combining observational data with theoretical models. J. N. Bahcall & R. M. Soneira (1980) developed the first consistent model using star count data, revealing that the Milky Way consists of two Galactic components: a thin disk with a scale height of 325 pc and a halo. However, G. Gilmore & N. Reid (1983) proposed a three-component model, adding a thick disk to account for discrepancies in the data. According to G. Gilmore & N. Reid (1983) the thick disk has a scale height of 1450 pc for $1 < z \text{ (kpc)} < 5$ distance range and they suggested that the thick disk contributes 2% of the thin disk's density in the solar neighborhood.

Subsequent studies have further refined the Galactic model parameters of the Milky Way. D. K. Ojha et al. (1996) estimated that the vertical scale height of stars fainter than $M_V = 3.5$ mag in the thin disk was $h_z = 260 \pm 50$ pc, while in the thick disk scale height was $h_z = 760 \pm 50$ pc, representing 7.4% of the local density of the thin disk. These findings have been instrumental in shaping our current understanding of the multicomponent structure of the Galaxy. R. Buser et al. (1998, 1999) studied star counts using RGO photometric data of star fields in different directions of the Galaxy within the scope of the Basel Palomar-Schmidt program. As a result, they estimated the local density of the thick disk to be $5.9\% \pm 3\%$ and the scale length and scale height of the thick disk to be 3.0 ± 1.5 kpc and 0.91 ± 0.3 kpc, respectively. Although the presence of the thick disk was well established, the Galaxy model parameters of the three Galactic components, especially the thick disk population, could not be given clearly (B. Chen et al. 2001; M. H. Siegel et al. 2002).

With the development of technology, the common use of CCDs in astronomical observations has enabled fainter stars to be analyzed (e.g., P. B. Hall et al. 1996; S. Karaali et al. 2003). Thanks to the systematic sky surveys that started in the 2000s, the study of the three-dimensional structure of the Galaxy has entered a new era. S. Karaali et al. (2004), who analyzed the SA114 star field with the 2.5 m INT telescope using $u'_{RGO} g'_{RGO} r'_{RGO} i'_{RGO} z'_{RGO}$ filters,³ showed that the scale height of the thin-disk population increased from 265 pc to 495 pc as the absolute magnitude changed from bright to faint. Additionally, the density of the thick disk component in the solar neighborhood decreased from 9.5% to 5.2% with the same



Original content from this work may be used under the terms of the [Creative Commons Attribution 4.0 licence](https://creativecommons.org/licenses/by/4.0/). Any further distribution of this work must maintain attribution to the author(s) and the title of the work, journal citation and DOI.

³ RGO denotes Royal Greenwich Observatory.

change in absolute magnitude. However, they also found that the halo star density in the solar vicinity was in the range of 0.02%–0.05% and the halo axial ratio was $c/a = 0.7$. S. Bilir et al. (2006b), who studied the ELAIS star field with photometric data from the INT 2.5 m telescope, obtained the scale height for the thin disk as $H = 269 \pm 8$ pc, the star density of the thick disk as 6.46% and the scale height as $H = 760 \pm 60$ pc, and the star density of the halo in the solar neighborhood as 0.08% and the axis ratio as $c/a = 0.55 \pm 0.20$. Photometric studies of relatively small star fields in different directions of the Galaxy have shown that unique parameters describing the Galactic population have not yet been obtained (see also, C. Du et al. 2003; S. Bilir et al. 2006a, 2006c; S. Ak et al. 2007a, 2007b; H.-F. Wang et al. 2018; Ž. Chrobáková et al. 2020; Y. Yu et al. 2021).

M. Jurić et al. (2008) provided Galaxy model parameters for three Galactic populations from the analysis of Sloan Digital Sky Survey (SDSS, D. G. York & J. Adelman 2000) photometric data of about 48 million stars in a region of about 6500 square degrees of sky. As a result of the analyses of M dwarf stars in the solar neighborhood, the scale length and scale height of the thin disk were determined as $h_1 = 2600$ pc and $H_1 = 300$ pc, respectively. In addition, the local stellar density, scale length, and scale height of the thick disk were found as 12%, $h_2 = 3600$ pc, and $H_2 = 900$ pc, respectively, while the local stellar density and axis ratio of the halo were estimated as 0.5% and $c/a = 0.64$, respectively. Similar studies have also been conducted with different objects at high Galactic latitudes. A. Cabrera-Lavers et al. (2007) analyzed the Two Micron Sky Survey (2MASS, M. F. Skrutskie et al. 2006) photometry data of red-clump stars ($0^\circ < l \leq 360^\circ$, $60^\circ < b \leq 70^\circ$), which were good distance indicators, while S. Bilir et al. (2008a) studied the SDSS photometric data of main-sequence stars with different absolute magnitude intervals in the almost sky region ($0^\circ < l \leq 360^\circ$, $60^\circ < b \leq 65^\circ$). Although both studies were carried out in nearly the same region of the sky, it was shown that the Galaxy model parameters for Galactic populations were defined over a wide range of parameters.

The wide range of Galaxy model parameters may be attributed to many factors, with the main reasons organized as follows: (i) Galaxy model parameters depend on the Galactic latitude/longitude of the sources (S. Bilir et al. 2006a, 2006b, 2006c; S. Ak et al. 2007a; A. Cabrera-Lavers et al. 2007; E. Yaz & S. Karaali 2010; E. Yaz Gökçe et al. 2015); (ii) Galaxy model parameters depend on the luminosity class of stars with wide absolute magnitude ranges (S. Karaali et al. 2004; S. Bilir et al. 2006a, 2006b, 2006c; A. Cabrera-Lavers et al. 2007; S. Bilir et al. 2008a); (iii) Galaxy model parameters have different values in different space volumes depending on the completeness limits (S. Karaali et al. 2007); (iv) in the star counting method, the distances of the stars were determined by different photometric parallax calibrations (S. Karaali et al. 2005; S. Bilir et al. 2005, 2008b, 2009); and (v) depending on the stellar sample used in the Galaxy model parameter determination studies, the morphology of the density functions used to separate the thin disk, thick disk, and halo components of the Galaxy varies. In the literature, studies have demonstrated that stars with bright absolute magnitudes are well represented by an exponential law, whereas samples of stars with faint absolute magnitudes are more accurately described by the sec or sech² law (S. Bilir et al. 2006b, 2006c; S. Karaali et al. 2009; E. Yaz & S. Karaali 2010; E. Yaz Gökçe et al. 2015).

The Galaxy model parameters cannot be expressed uniquely for the reasons listed above.

The Gaia mission aims to create a complex three-dimensional map of the Milky Way through precise measurements of the positions, distances, and motions of more than a billion stars (Gaia Collaboration et al. 2016). For this purpose, the Gaia satellite was launched by the European Space Agency (ESA) in 2013. The Gaia catalog, with three main data releases so far, contains astrometric data such as positions, trigonometric parallax, and proper motion components of 1.8 billion stars; photometric data such as magnitude in the G , G_{BP} , and G_{RP} bands defined at optical wavelengths; and spectroscopic data such as atmospheric model parameters and radial velocity measurements from low-resolution spectra (Gaia Collaboration et al. 2023). With these features, the Gaia database allows us to study the structure of the Milky Way in detail.

Using precise astrometric data from the Gaia EDR3 (Gaia Collaboration et al. 2021a) catalog, Gaia Collaboration et al. (2021b) obtained space densities and luminosity functions by classifying 331 312 stars within 100 pc into dwarf, giant, and white dwarf. As a result of this study, the luminosity functions of main-sequence stars have been obtained in the absolute magnitude $-1 \leq M_G$ (mag) ≤ 20 interval and the luminosity functions of red giant stars have been obtained for the range of $-1 < M_G$ (mag) ≤ 4 . Especially in the range $0 < M_G$ (mag) ≤ 1 , where red giant stars were found, the luminosity function as $\Theta = 1.9 \pm 0.1 \times 10^{-4}$ stars pc⁻³ mag⁻¹ was found to increase significantly. Since the results were obtained for a very limited volume of space, other Galaxy model parameters such as the scale length and scale height could not be calculated.

The study of evolved stars in the solar neighborhood with precise data provided by the Gaia satellite was of great importance in estimating the Galaxy model parameters of the thin-disk population. In this study, we used photometric and astrometric data from the Gaia satellite to identify evolved stars within 1 kpc of the Sun using a color–magnitude diagram. The Galaxy model parameters were estimated by dividing the selected evolved stars into different Galactic latitude and longitude intervals, and different absolute magnitude ranges.

2. The Density Law of the Thin Disk

Disk structures in Galaxy models, especially in the studies of Galactic disks, are usually parameterized in cylindrical coordinates through radial and vertical exponential functions. This parameterization allows for a more precise representation of the density distribution along both the radial and vertical axes related to the Galactic plane. The double exponential density law for the thin disk of the Milky Way is represented as follows,

$$D(x, z) = n \times \exp\left(-\frac{|z + z_0|}{H}\right) \times \exp\left(-\frac{(x - R_0)}{h}\right), \quad (1)$$

where x is the planar distance from the Galactic center, z is the distance of stars from the Galactic plane, z_0 distance of the Sun from the Galactic plane (15 pc, M. Cohen 1995; P. L. Hammersley et al. 1995), R_0 is the solar distance to the Galactic center (8 kpc, S. R. Majewski 1993), n is the normalized local density, and h and H are the scale length and scale height of the thin-disk component, respectively. The following equation calculates the planar distance from the

Galactic center,

$$x = [R_0^2 + (z/\tan b)^2 - 2R_0(z/\tan b)\cos l]^{1/2}, \quad (2)$$

where l and b are the Galactic longitude and latitude of the star field under study. Since this study analyzes evolved stars in the solar neighborhood ($d \leq 1$ kpc), the sample does not reach far enough to determine the scale length of the thin disk. Therefore, Equation (1) is simplified to determine only the space densities and scale heights of thin disk stars,

$$D(z) \cong n \times \exp\left(-\frac{|z + z_0|}{H}\right). \quad (3)$$

3. Data and Analyses

The Gaia Third Data Release (Gaia DR3, Gaia Collaboration et al. 2023) contains astrometric, photometric, and spectroscopic data from 34 months of observations of 1.8 billion sources. The precision of the trigonometric parallaxes in the database varies depending on the G -apparent magnitudes. The trigonometric parallax errors were $\sigma_\varpi = 0.03$ mas for $G < 15$ mag, $\sigma_\varpi = 0.07$ mas for $G = 17$ mag, and $\sigma_\varpi = 0.5$ mas for $G = 20$ mag, which were given in the Gaia DR3 database. Similarly, the uncertainties of the proper motion measurements were 0.03 mas yr⁻¹ for $G < 15$ mag, 0.07 mas yr⁻¹ for $G = 17$ mag, and 1.40 mas yr⁻¹ for $G = 21$ mag.

This study uses the photometric and astrometric data of the evolved stars in Gaia DR3 database (Gaia Collaboration et al. 2023) to determine the Galaxy model parameters of the thin-disk population. The photometric and astrometric data in the `gaiadr3.gaia_source` table⁴ were used to select the stars in the 1 kpc heliocentric space volume. To determine the distances of the stars more accurately and sensitively, it was considered appropriate to consider single stars with relative parallax errors $\sigma_\varpi/\varpi \leq 0.10$ in the Gaia DR3 database. In addition, the value of 0.017 mas was taken into account for the global parallax offset in the trigonometric parallax data of the selected stars (L. Lindegren et al. 2021). For the selection of single stars in the stellar sample, the renormalised unit weight error (RUWE) parameters given in the Gaia DR3 database for each source were chosen such as $\text{RUWE} \leq 1.4$ (e.g., A. Castro-Ginard et al. 2024). Considering the main points mentioned above, the following code was written in the SQL section of the Gaia DR3 database and the data providing these conditions were listed.

```

SELECT *
FROM gaiadr3.gaia_source as gaia
WHERE gaia.parallax_over_error >=10 AND
      (gaia.parallax+0.017) >=1 AND
      RUWE <= 1.4

```

This SQL query resulted in 39,099,903 stars within the 1 kpc distance that have relative parallax errors of less than 0.10. The distances of the stars were calculated with the conventional inverse parallax relation, $d(\text{pc}) = 1000/\varpi$ (mas), using Gaia DR3 data. Photometric Gaia bands were dereddened using the following methodology.

⁴ https://gaia.aip.de/metadata/gaiadr3/gaia_source/

3.1. Photometric Color Excess Determination

In this study, the dust map of E. F. Schlafly & D. P. Finkbeiner (2011) was used to correct the photometric data of selected stars from the Gaia DR3 catalog for the extinction effect of the interstellar medium. The V -band extinction ($A_\infty(V)$) values in the line of the stars (l, b) up to the Galactic boundary were determined with the help of the Python library `mw dust` (J. Bovy et al. 2016a). Since the stars in this study were not located at the Galactic boundary, the V -band extinction value ($A_d(V)$) determined from the dust map of E. F. Schlafly & D. P. Finkbeiner (2011) needs to be recalculated for the distance between the Sun and stars. The relation of J. N. Bahcall & R. M. Soneira (1980) was used to determine the reduced V -band extinction,

$$A_d(V) = A_\infty(V) \times \left[1 - \exp\left(\frac{-|d \times \sin b|}{H}\right)\right], \quad (4)$$

where b is the Galactic latitude of the star, d is the distance of the star which is calculated from the corrected trigonometric parallax measurements of the star in the Gaia DR3 catalog with the relation $d(\text{pc}) = 1000/\varpi$ (mas), H is the scale height of the dust ($H = 125^{+17}_-7$ pc, D. J. Marshall et al. 2006), $A_\infty(V)$ is the V -band extinction measured from the star line to the Galaxy boundary, and $A_d(V)$ is the extinction value for the distance between the Sun and star.

The selective absorption coefficients of J. A. Cardelli et al. (1989) were used to correct the photometric bands in the Gaia DR3 catalog for the effect of interstellar extinction. In this study, the $R_V = 3.1$ curve of J. A. Cardelli et al. (1989) was used to determine the extinction coefficients of these filters. The effective wavelengths of Gaia passbands for G , G_{BP} , and G_{RP} are 6390.21 Å, 5182.58 Å, and 7825.05 Å, respectively, the corresponding A_λ/A_V values are 0.83627, 1.08337, and 0.63439, respectively (see also, R. Canbay et al. 2023). Accordingly, the relations that should be used for de-reddening three Gaia passbands are as follows:

$$\begin{aligned} G_0 &= G - A_G = G - 0.83627 \times A_d(V) \\ (G_{\text{BP}})_0 &= G_{\text{BP}} - A_{G_{\text{BP}}} = G_{\text{BP}} - 1.08337 \times A_d(V) \\ (G_{\text{RP}})_0 &= G_{\text{RP}} - A_{G_{\text{RP}}} = G_{\text{RP}} - 0.63439 \times A_d(V). \end{aligned} \quad (5)$$

The absolute magnitudes M_G of stars were calculated using the distance modulus formula $G - M_G = 5 \times \log(1000/\varpi) - 5 + A_G$, where ϖ is the trigonometric parallax with global zero-point corrected. The V -band extinctions from the E. F. Schlafly & D. P. Finkbeiner (2011) dust maps for the selected stars are shown in the upper panel of Figure 1, and those calculated for the distance between the Sun and the star in V -band absorption are represented in the lower panel of Figure 1.

3.2. Selection of Evolved Stars

The color–magnitude diagram (CMD) of 39,099,903 stars of different luminosity classes in a heliocentric 1 kpc volume of space is shown in Figure 2. To better represent the star densities on the $M_G \times (G_{\text{BP}} - G_{\text{RP}})_0$ CMD, the stars were colored according to their number densities. The main-sequence, evolved, and white dwarf stars in the sample have different positions on the CMD and can be easily distinguished by the eye. In addition, the spectral types of the stars given by the web

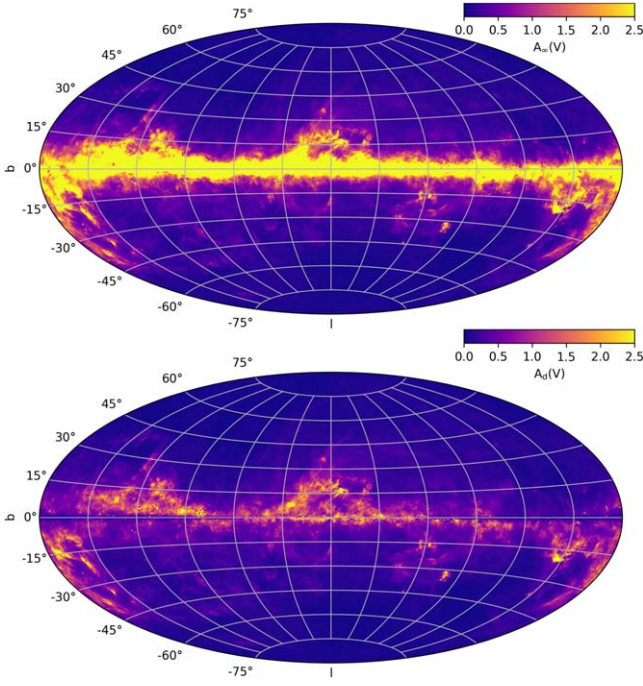


Figure 1. V-band extinction $A_{\infty}(V)$ values from the dust maps of E. F. Schlafly & D. P. Finkbeiner (2011; upper panel) and the distance between Sun and stars reduced $A_d(V)$ values (lower panel).

page of Mamajek⁵ for Gaia photometry are shown at the lower part of Figure 2. Considering these properties of the star groups, main-sequence stars and evolved stars are separated by green and red dashed lines in Figure 2, respectively. The color indices and absolute magnitudes of main-sequence stars span $-1 < (G_{BP} - G_{RP})_0$ (mag) < 4 and $-2 < M_G(\text{mag}) < 15$, while evolved stars cover $0.8 < (G_{BP} - G_{RP})_0$ (mag) < 2.2 and $-3 < M_G(\text{mag}) < 4$ intervals. The number of evolved stars in the area bounded by the blue dashed lines on the figure showing the evolved star region was identified as 776,246. This evolved star region is also composed of subevolved classes, such as red giant branch (RGB; $-3 < M_G(\text{mag}) < 4$), red-clump (RC; $M_G = 0.5$, $G_{BP} - G_{RP})_0 = 1.2$ mag), secondary red-clump ($M_G = 0.6$, $G_{BP} - G_{RP})_0 = 1.1$ mag), and asymptotic giant branch (AGB) bump stars (see also, Gaia Collaboration et al. 2018).

3.3. Spatial Distributions and Completeness Limits

Determining distance and completeness limits for the objects used in calculating the Galaxy model parameters is critical for ensuring accuracy and precision for the unique parameters. In this study, the distances of selected evolved stars from the Sun were determined by applying the trigonometric parallax data provided in the Gaia DR3 catalog to the standard distance-parallax relation, $d(\text{pc}) = 1000/\varpi$ (mas), where d is the distance and ϖ is the corrected trigonometric parallax. While the relative parallax error (σ_{ϖ}/ϖ) for the stars in the selected sample was set at 0.10, it was found that the most reliable distances were constrained within a relative parallax error of 0.02. Within this limit, approximately 86% of the selected evolved stars were included. By applying this constraint to the star sample, the total number of stars considered was 671,600. To investigate the spatial distribution of the sample, we

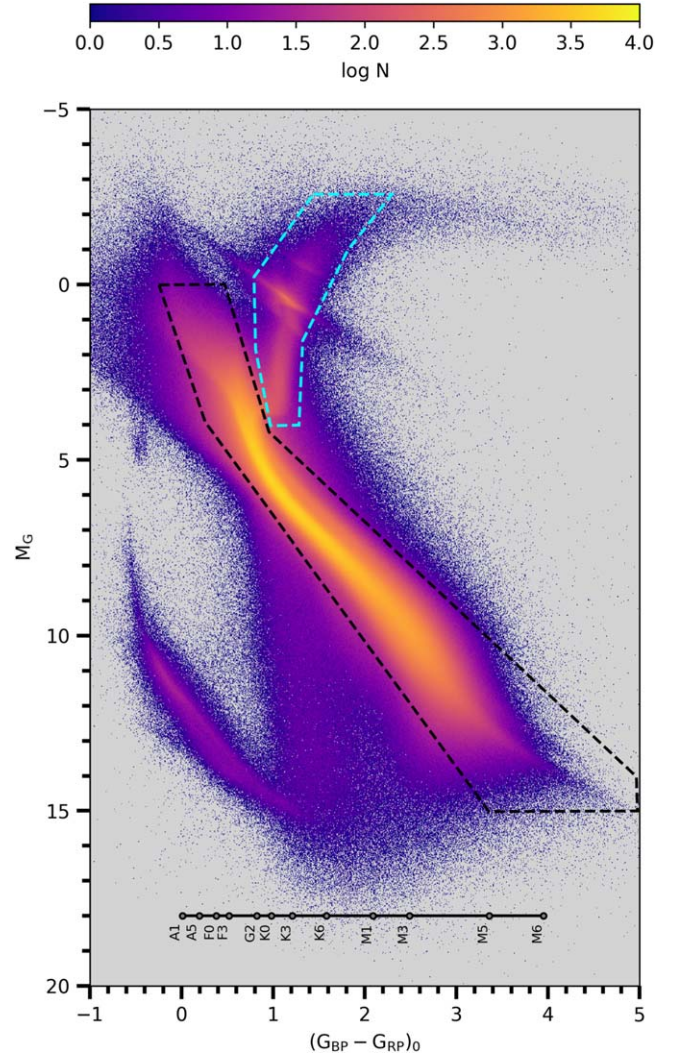


Figure 2. $M_G \times (G_{BP} - G_{RP})_0$ CMD of a sample of 39,099,903 stars within the solar neighborhood. Main-sequence and evolved stars occupy the black dashed and blue dashed regions, respectively. The star clump at the lower left-hand part of the diagram is the white dwarf region. Spectral types concerning the dereddened color index are shown in the bottom part of the diagram.

calculated the heliocentric rectangular Galactic coordinates (X toward the Galactic Center, Y Galactic rotation, Z North Galactic Pole). Figure 3 displays the projected positions on the Galactic plane (X, Y) and the Galactic plane perpendicular to it (X, Z). In particular, the stellar density in the $Y \times X$ plane shows a homogeneous distribution of stars around the Sun, while in the $Z \times X$ plane there was a slight deviation from the homogeneous distribution.

To determine the completeness distances of the stars in the sample, the apparent and absolute magnitudes of the stars must be known. The apparent and absolute magnitudes of the selected evolved stars were in the $3 < G(\text{mag}) \leq 22$ and $-1 < M_G(\text{mag}) \leq 4$ intervals, respectively. In this study, the completeness limits of the stars in the volume of space in which they are located were determined by dividing the stars into intervals of unit absolute magnitude. The following relations were used to estimate the completeness distance limits,

$$\begin{aligned} d_{\min} &= 10^{[(G_1 - M_1 + 5 - A_G)/5]} \\ d_{\max} &= 10^{[(G_2 - M_2 + 5 - A_G)/5]}. \end{aligned} \quad (6)$$

⁵ https://www.pas.rochester.edu/~emamajek/EEM_dwarf_UBVIJHK_colors_Teff.txt

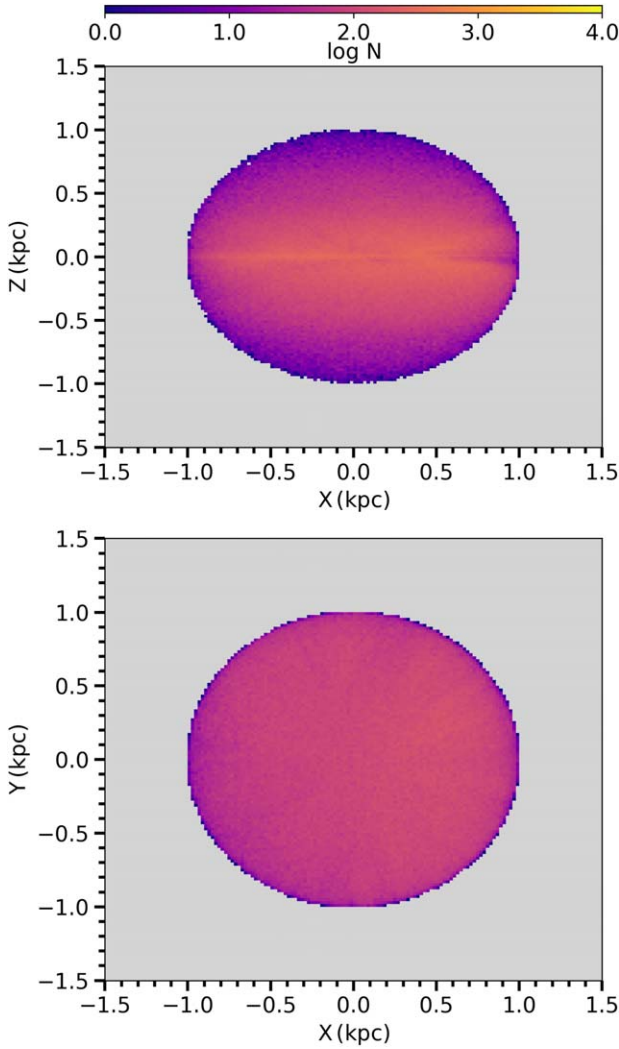


Figure 3. Spatial distributions of 671,600 evolved stars whose astrometric data were precisely selected from the Gaia DR3 catalog: $Z \times X$ (upper panel) and $Y \times X$ (bottom panel). The color scale indicates the density of the star count.

Here, G_1 and G_2 represent the brightest and faintest dereddened apparent magnitudes within the specified range of absolute magnitudes (e.g., $M_1 < M_G \leq M_2$), while d_{\min} and d_{\max} correspond to the minimum and maximum limiting distances, respectively.

To evaluate the completeness limits of the star sample, we constructed a diagram representing the absolute magnitude in the Gaia G -band in Figure 4, with completeness limits marked at intervals of 0.25 mag. The vertical white lines in Figure 4 signify the distance at which completeness begins for each absolute magnitude interval. We determined these starting points by identifying the initial 0.5% slice of the G -band apparent magnitude distribution within each absolute magnitude bin. Additionally, the black solid lines labeled with turquoise numbers represent the G -apparent magnitudes, while the black dashed lines denote increments of 0.5 mag between two consecutive G -apparent magnitudes. The orange dashed lines further subdivide these increments, indicating the 0.25 and 0.75 mag levels. For subsequent calculations of space density, data points lying below this completeness threshold were excluded from the sample. To determine the faint limiting magnitude of the evolved stars in the sample, the G -apparent

magnitudes of stars with different absolute magnitudes at a distance of $d = 1$ kpc were used. Accordingly, the G -apparent magnitudes corresponding to the G -absolute magnitude of -1 and 4 were determined to be 9 and 14 mag, respectively. Moreover, since the faint limiting magnitude of the photometric data provided by the Gaia satellite is $G = 20.5$ mag (e.g., S. Gokmen et al. 2023; S. Tasdemir & T. Yontan 2023; T. Yontan & R. Canbay 2023), the faint limiting magnitude calculated in this study can be reliable. Based on the analysis, the number of evolved stars within the completeness limits was determined as 671,600 by applying Equation (6) to the sample.

3.4. Space-density Profiles

To calculate the space density of stars located in a star field direction, space volumes were defined by considering different distance intervals from the Sun, and the number of stars in these volume elements was then determined. The expression used to calculate space density is given in Equation (7),

$$D = \frac{N}{\Delta V_{1,2}}. \quad (7)$$

Here, D represents the star density, while N is the number of stars. $\Delta V_{1,2}$ represents the space volume that was calculated using the following equation,

$$\Delta V_{1,2} = \left(\frac{\square}{3}\right) \left(\frac{\pi}{180}\right)^2 [d_2^3 - d_1^3]. \quad (8)$$

Here, \square is the size of the selected star field (square degree), and d_1 and d_2 represent two different distances from the Sun, respectively. In this study, to create the density profiles of stars centered on the Sun and located in the space volume $d \leq 1$ kpc, the evolved stars were divided into 200 pc distance intervals from the Sun. As stellar distances increase, space volumes grow, leading to underestimated calculations of space densities. To simultaneously show high and low stellar space densities, the relation $D^* = \log D + 10$ as presented in the literature was utilized in this study (see R. Fenkart & S. Karaali 1987). In addition, the centroid distance (d^*) of the partial volume ($\Delta V_{1,2}$) corresponding to distances $d_1 - d_2$ was used to generate the stellar density profiles:

$$d^* = \sqrt[3]{\frac{d_1^3 + d_2^3}{2}}. \quad (9)$$

3.5. Galaxy Model Parameters

This study aims to derive the parameters of the Galaxy model as a function of the Galactic coordinates (l , b) and the absolute magnitude (M_G). To accomplish this, evolved stars were segmented on a heliocentric celestial sphere categorized according to their Galactic latitude and longitude. The selected Galactic latitude intervals for north and south Galactic hemispheres were $25^\circ < |b| \leq 50^\circ$, $50^\circ < |b| \leq 75^\circ$, and $75^\circ < |b| \leq 90^\circ$, and the selected Galactic longitude intervals were $0^\circ < l \leq 60^\circ$, $60^\circ < l \leq 120^\circ$, $120^\circ < l \leq 180^\circ$, $180^\circ < l \leq 240^\circ$, $240^\circ < l \leq 300^\circ$, and $300^\circ < l \leq 360^\circ$. These choices created 18-star fields in the northern Galactic hemisphere and 18-star fields in the southern Galactic hemisphere, totaling the 36-star fields shown in Figure 5. The numbers starting with the number sign # in Figure 5 give the number of

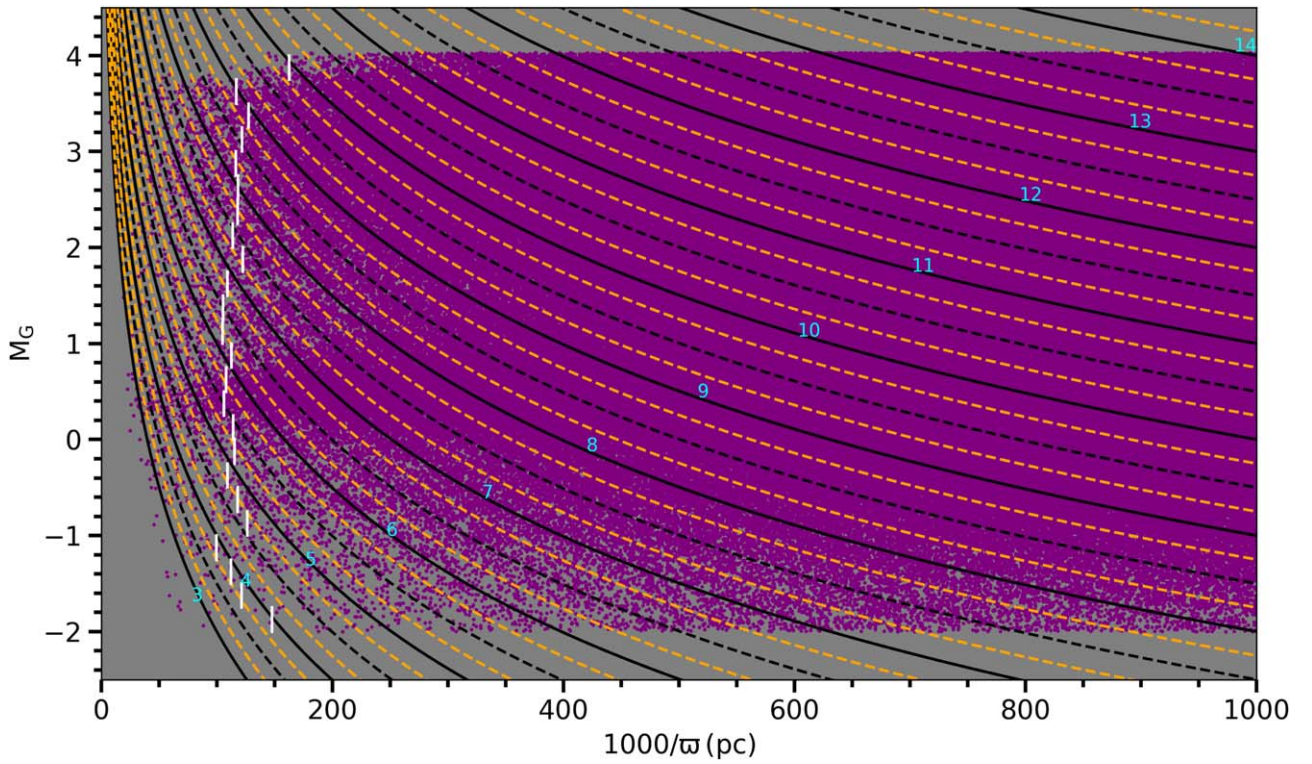


Figure 4. $M_G \times d$ diagram of evolved stars with $\sigma_\omega/\omega \leq 0.02$. White vertical lines are bright G -apparent magnitude limits for different M_G absolute magnitude intervals, and solid and dash curves also represent G -apparent magnitudes.

the star field. Since this study focuses on evolved stars located within 1 kpc of the Sun, stars situated in star fields with Galactic latitude $|b| \leq 25^\circ$ can reach a maximum distance of approximately 425 pc from the Galactic plane. This calculated value is slightly larger than the one scale height reported for the thin disk in the literature (see S. Karaali et al. 2004; S. Bilir et al. 2006b). To accurately and precisely determine the scale height of a Galactic population, stars in the star field must be within three to five scale heights of the Galactic plane. For this reason, the part of the sky with $|b| \leq 25^\circ$ and shown in blue on Figure 5 was removed from the sample, leaving 241,956 evolved stars.

To plot the space-density profiles of the star fields, the evolved stars in the sample were divided into five absolute magnitude intervals: $-1 < M_G(\text{mag}) \leq 0$, $0 < M_G(\text{mag}) \leq 1$, $1 < M_G(\text{mag}) \leq 2$, $2 < M_G(\text{mag}) \leq 3$, and $3 < M_G(\text{mag}) \leq 4$. Evolved stars in each absolute magnitude interval were classified according to their distance, divided into 200 pc distance intervals. The star space density in each distance range was obtained using Equation (7). The space volumes were then calculated using Equation (8) and the sizes of star fields for three different latitude zones as $25^\circ < |b| \leq 50^\circ$, $50^\circ < |b| \leq 75^\circ$, and $75^\circ < |b| \leq 90^\circ$ were calculated as about 1181, 687, and 117 degrees², respectively. In total, 180 space-density profiles were constructed within 36-star fields for five consecutive absolute magnitude intervals. The space-density profiles are fitted with a single-component density law to obtain the Galaxy model parameters of each star field.

Galaxy model parameters were determined by fitting the density law for the thin-disk population in Equation (3) to the observational density profiles calculated from the star field. To calculate the Galaxy model parameters, space densities

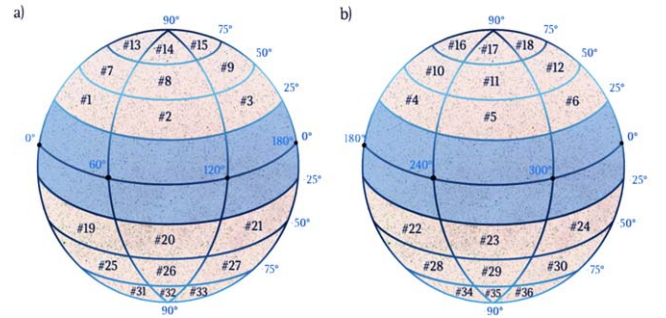


Figure 5. Heliocentric celestial sphere separated into 36-star fields based on the Galactic coordinates of evolved stars: (a) $0^\circ < l \leq 180^\circ$ and (b) $180^\circ < l \leq 360^\circ$.

were used in steps of 0.01 in the range $4 < D^* < 8$, and for the scale height steps of 1 pc in the interval $100 < H \text{ (pc)} < 1000$ were used. In this study, the parameters of the Galaxy model with the minimum chi-square (χ^2_{\min}) were considered in selecting the model that best represents the space-density profile.

This study requires modeling many star fields and space-density profiles obtained from stars of five consecutive absolute magnitude intervals in these fields. To save space in this paper, the analyses are shown in Figure 6 for evolved stars found at five absolute magnitude intervals in star field #01. The Galaxy model parameters estimated for the star fields as a result of the comparison of the observational space densities with the Galaxy model are listed in Table A1. Uncertainties of the estimated space density (D^*) and scale height (H) for the thin-disk population were given for $\pm 1\sigma$. Moreover, the estimated Galaxy model parameters for the 36-star fields are also listed in Table A1.

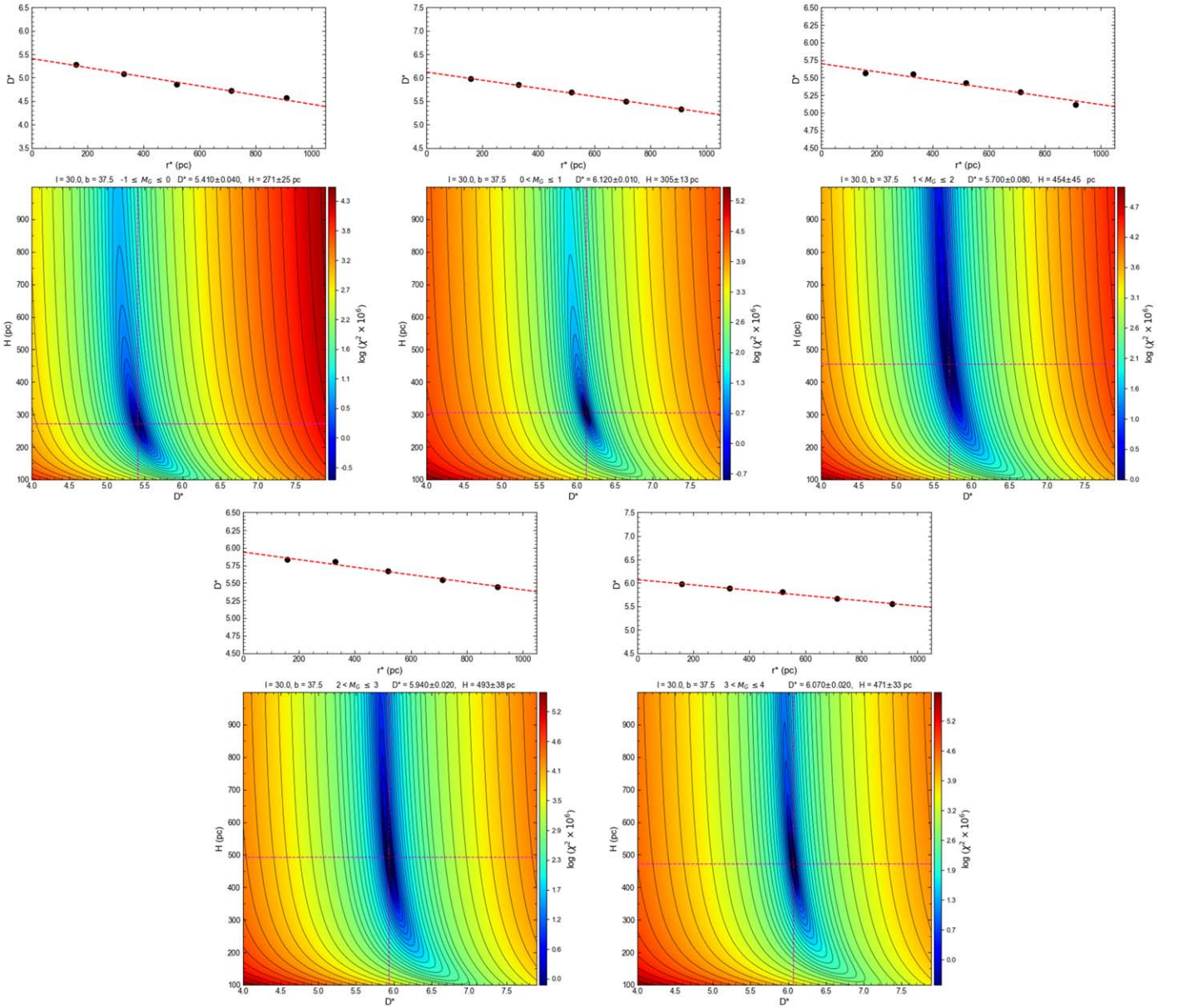


Figure 6. Stellar density profiles for five absolute magnitude intervals in star field #01 (upper panels) and variations of model parameters with χ^2 values (lower panels). The red lines in the upper panels show the Galaxy model fitted to the star density points, and the intersections of the red dashed lines represent the Galaxy model parameters with the minimum χ^2_{\min} value. The numerical values between the two panels are the central coordinates of the star field in the Galactic coordinate system, the absolute magnitude interval, the estimated space density, and the scale height.

4. Discussion and Conclusion

In this study, we determined the space densities and scale heights of the Galactic thin-disk population by analyzing the spatial distribution of evolved stars within a heliocentric volume extending to 1 kpc. For this purpose, a sample of 671,600 evolved stars was selected based on their positions in the Hertzsprung–Russell (HR) diagram, using photometric and astrometric data from the Gaia DR3 catalog. Each star in the sample had a relative parallax error of less than 0.02, ensuring reliable spatial measurements.

In this study, symmetric star fields from the northern and southern Galactic zones were jointly analyzed to refine the interpretation of the Galaxy model parameters calculated across 36-star fields and within five absolute magnitude intervals.

Initially, the space density values derived for the thin disk within symmetric zones were prioritized. To achieve this, the variation in space densities of star fields as a function of their absolute magnitudes in the $D^* \times M_G$ planes is illustrated on the left-hand side of Figure A1. Each panel also displays the luminosity functions of evolved stars within a 100 pc space volume (Gaia Collaboration et al. 2021b). The space densities (D^*) corresponding to the absolute magnitude intervals of $-1 < M_G \text{ (mag)} \leq 0$, $0 < M_G \text{ (mag)} \leq 1$, $1 < M_G \text{ (mag)} \leq 2$, $2 < M_G \text{ (mag)} \leq 3$, and $3 < M_G \text{ (mag)} \leq 4$ were calculated as 5.41, 6.09, 5.76, 5.91, and 6.07, respectively, based on the relation $D^* = \log D + 10$. Overall, the calculated space densities for these five absolute magnitude intervals across star fields within three distinct Galactic latitude zones align closely with the luminosity function obtained for evolved stars

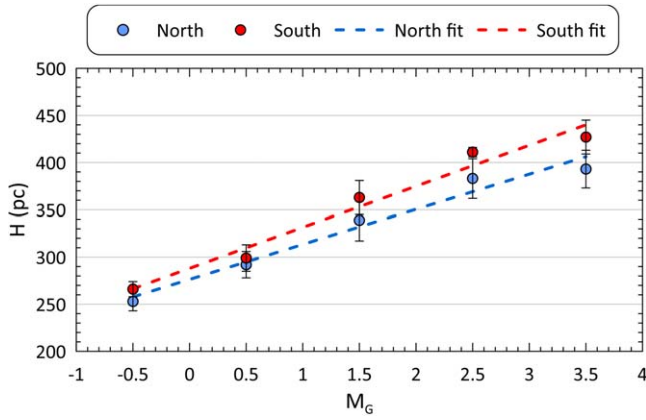


Figure 7. The variation in scale heights calculated for evolved stars concerning their absolute magnitudes across both Galactic hemispheres.

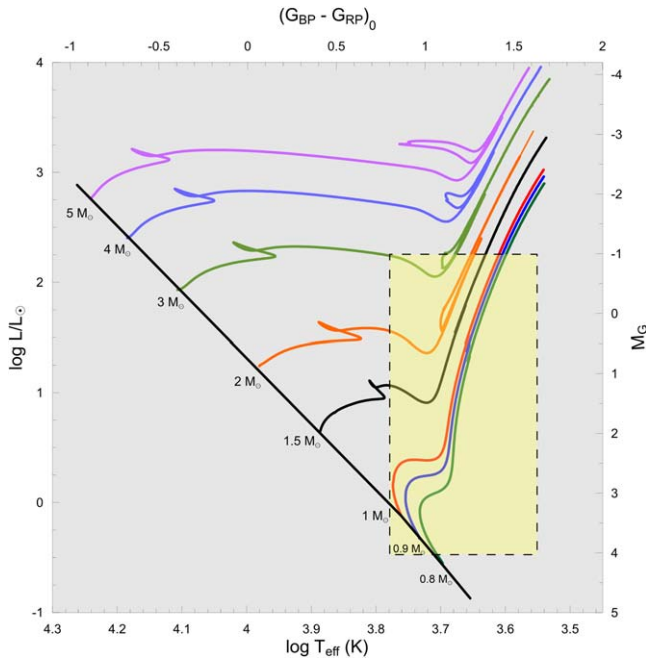


Figure 8. The positions of the PARSEC mass tracks of main-sequence stars of different masses on the CMD. The curves with different colors indicate different masses, and the dashed lines indicate the region where the evolved stars studied were located.

by Gaia Collaboration et al. (2021b). The consistency between space densities calculated within a 1 kpc space volume and those in existing luminosity function literature further indicates that the estimated scale height for the thin-disk population remains unaffected by parameter degeneracy.

The Galaxy model parameters of the thin disk were estimated under the assumption that the evolved stars in a 1 kpc space volume predominantly belong to the thin disk in this study. However, it is well-established that the solar neighborhood contains stars from different Galactic populations. To quantify the potential impact of these populations on the results, a Monte Carlo simulation was conducted. For this simulation, a star field was selected for testing and was modeled using a single exponential law. This model assumes that the local space density of the thick disk varies $0 < n$ (%) ≤ 15 and the scale height of the thick disk varies $550 \leq H$ (pc) ≤ 1500 . For the halo population, it is assumed that the local space density is between 0.1% and 0.2%. These parameter

ranges are consistent with values reported in the literature and are listed in Table 1 provided by S. Bilir et al. (2006b). The analysis focused on the space densities in the absolute magnitude range $0 < M_G$ (mag) ≤ 1 , dominated by red-clump stars in the selected star field (#01). Using a Monte Carlo simulation with 10,000 trials, the Galaxy model parameters for the thick disk and halo populations were randomly selected in each trial. Observational data were subsequently remodeled by reconstructing the exponential density law of the thin disk. The results of the simulation reveal that the scale height of the thin-disk population varies in the range $295 \leq H$ (pc) ≤ 310 , with the most probable value determined as $H = 303 \pm 3$ pc based on a Gaussian fit to the distribution. This value is in excellent agreement with the 305 ± 13 pc obtained in this study without discriminating between different stellar populations (see Table 1). These findings indicate that the scale height of the thin disk, as derived from evolved stars within a 1 kpc space volume, is minimally affected by the presence of stars from other Galactic populations. This result underscores the robustness of the adopted method and provides a reliable estimate for the thin disk’s vertical structure.

The variation in scale heights of evolved stars in the thin-disk population is analyzed for their Galactic coordinates and absolute magnitude intervals. The methodological steps used to interpret the space-density parameters have likewise been applied to the determination of the scale height parameter. For this purpose, the scale heights estimated for evolved stars in the five absolute magnitude intervals covering star fields in both the northern and southern Galactic hemispheres are provided in Table 1. The right-hand side of Figure A1 illustrates the range of scale heights for different absolute magnitude intervals in these symmetric star fields, which spans from $200 < H$ (pc) < 600 . Notably, an increasing trend is observed in scale heights from brighter to fainter absolute magnitudes within each Galactic latitude zone, a trend that similarly appears for symmetric star fields at equivalent latitudes. This trend is further evident from the median scale height values calculated for each absolute magnitude interval in the bottom row of Table 1. The variation in median scale heights calculated for evolved stars concerning their absolute magnitudes in both Galactic hemispheres is presented in Figure 7. It has been seen that, as the absolute magnitudes of stars transition from brighter to fainter, the scale height increases from 250 to 430 pc. In addition, the scale heights calculated for evolved stars in the southern hemisphere are slightly larger than those obtained for stars in the northern hemisphere. Considering the trend observed in the data from both hemispheres, linear fits have been applied, resulting in the following relations,

$$\begin{aligned} H_{\text{North}} &= 37.1 \times M_G + 276 \quad (R^2 = 0.968) \\ H_{\text{South}} &= 43.4 \times M_G + 288 \quad (R^2 = 0.970). \end{aligned} \quad (10)$$

The relationships calculated for both Galactic hemispheres exhibit a high degree of correlation. Although the slopes of the two relationships are nearly identical, there is a difference in the zero-point of 12 pc between the southern and northern Galactic hemispheres.

It can be seen from Figure 2 that the red-clump stars, which stand out as a dense population among the evolved stars analyzed in this study, are located in the absolute magnitude $0 < M_G$ (mag) ≤ 1 interval. The scale heights of red-clump stars in the northern and southern Galactic hemispheres were also estimated as $H_{\text{north}} = 292 \pm 14$ and $H_{\text{south}} = 299 \pm 14$ pc,

Table 1
Scale Heights Estimated for Five Different Absolute Magnitude Intervals in the 36-star Fields

Field	Absolute Magnitude Intervals					Field	Absolute Magnitude Intervals				
	$-1 < M_G \leq 0$ H (pc)	$0 < M_G \leq 1$ H (pc)	$1 < M_G \leq 2$ H (pc)	$2 < M_G \leq 3$ H (pc)	$3 < M_G \leq 4$ H (pc)		$-1 < M_G \leq 0$ H (pc)	$0 < M_G \leq 1$ H (pc)	$1 < M_G \leq 2$ H (pc)	$2 < M_G \leq 3$ H (pc)	$3 < M_G \leq 4$ H (pc)
#01	271 ± 25	305 ± 13	454 ± 45	493 ± 38	471 ± 33	#19	288 ± 28	351 ± 19	392 ± 31	440 ± 05	555 ± 38
#02	269 ± 29	287 ± 15	382 ± 31	450 ± 17	411 ± 26	#20	254 ± 08	323 ± 16	397 ± 38	487 ± 05	440 ± 35
#03	242 ± 08	292 ± 48	315 ± 04	371 ± 24	344 ± 03	#21	323 ± 14	289 ± 12	340 ± 26	431 ± 04	366 ± 03
#04	277 ± 19	293 ± 12	271 ± 17	350 ± 33	305 ± 17	#22	274 ± 08	301 ± 16	352 ± 29	413 ± 04	315 ± 09
#05	251 ± 07	313 ± 02	319 ± 21	362 ± 03	341 ± 20	#23	295 ± 10	334 ± 15	448 ± 45	396 ± 27	394 ± 32
#06	264 ± 07	339 ± 19	396 ± 32	405 ± 01	395 ± 20	#24	335 ± 40	374 ± 18	401 ± 05	408 ± 04	418 ± 21
#07	272 ± 28	287 ± 11	368 ± 09	342 ± 02	405 ± 21	#25	300 ± 27	307 ± 05	384 ± 08	458 ± 04	476 ± 03
#08	252 ± 21	298 ± 13	365 ± 23	431 ± 26	382 ± 21	#26	225 ± 06	288 ± 02	365 ± 09	394 ± 10	428 ± 18
#09	238 ± 24	284 ± 40	308 ± 16	382 ± 35	377 ± 17	#27	221 ± 06	295 ± 14	357 ± 35	364 ± 03	406 ± 29
#10	272 ± 27	289 ± 14	324 ± 22	377 ± 20	357 ± 19	#28	258 ± 07	259 ± 02	343 ± 24	392 ± 03	357 ± 02
#11	238 ± 07	283 ± 11	317 ± 18	383 ± 20	393 ± 24	#29	299 ± 08	325 ± 30	394 ± 36	462 ± 40	442 ± 27
#12	253 ± 01	297 ± 15	346 ± 23	389 ± 34	392 ± 09	#30	357 ± 11	351 ± 19	404 ± 09	462 ± 04	452 ± 18
#13	201 ± 05	292 ± 39	315 ± 22	378 ± 08	433 ± 40	#31	220 ± 07	280 ± 13	422 ± 12	319 ± 05	392 ± 08
#14	214 ± 05	295 ± 47	331 ± 22	393 ± 21	495 ± 45	#32	253 ± 10	319 ± 30	278 ± 02	435 ± 38	435 ± 25
#15	220 ± 07	300 ± 14	362 ± 20	459 ± 29	487 ± 13	#33	201 ± 05	274 ± 02	288 ± 06	392 ± 36	426 ± 10
#16	253 ± 10	274 ± 11	348 ± 35	419 ± 11	414 ± 22	#34	273 ± 08	276 ± 12	318 ± 07	364 ± 09	404 ± 35
#17	294 ± 09	281 ± 41	274 ± 02	378 ± 32	363 ± 18	#35	246 ± 06	296 ± 14	361 ± 27	353 ± 19	484 ± 04
#18	219 ± 22	269 ± 10	355 ± 35	379 ± 09	389 ± 15	#36	204 ± 05	272 ± 12	299 ± 05	489 ± 13	439 ± 11
Median	253 ± 10	292 ± 14	339 ± 22	383 ± 21	393 ± 20	Median	266 ± 08	299 ± 14	363 ± 18	411 ± 05	427 ± 18

respectively, as given in Table 1. When the scale heights of the red-clump stars in both Galactic hemispheres and the weighted average of their errors were calculated, the scale height of the red-clump stars in the solar neighborhood was determined to be $H = 295 \pm 10$ pc. Although this result is slightly larger than the scale height values of $150 < H$ (pc) < 300 obtained by A. Cabrera-Lavers et al. (2007), who estimated the Galaxy model parameters for the thin-disk population from 2MASS photometric data of red-clump stars at high Galactic latitudes, it is in good agreement with the scale height of $H = 280$ pc determined by J. Bovy et al. (2016b) from their analysis of 14,699 red-clump stars selected from the APOGEE survey.

The space densities obtained from these star fields align closely with those observed in the solar neighborhood. However, the observed dependency of scale height on Galactic coordinates and absolute magnitude intervals indicates the need for further investigation to clarify the underlying causes of this variation. In this study, the observed variations in scale height were not attributed to parameter degeneracy, as demonstrated by the consistency of space densities with those of the solar neighborhood. The smaller scale heights of evolved stars with bright absolute magnitudes indicate that these systems predominantly consist of younger stars. To address this analysis, we employed the Padova and Trieste Stellar Evolution Code (PARSEC) stellar evolution models (A. Bressan et al. 2012; J. Tang et al. 2014; Y. Chen et al. 2015). Specifically, we considered mass tracks for solar-metallicity stars with heavy element abundance $Z = 0.014$ and helium abundance $Y = 0.273$. From these stellar evolution models, we selected eight theoretical stars with masses ranging from $0.8 \leq M/M_{\odot} \leq 5$. These theoretical stars, which evolved from the main sequence to advanced evolutionary stages, were depicted on the $M_G \times (G_{BP} - G_{RP})_0$ CMD, as shown in Figure 8. The associated luminosity (L/L_{\odot}) and temperature ($\log T_{\text{eff}}$) are displayed on the upper and right-hand axes of the CMD. Based on the Gaia color index and the absolute magnitudes of the evolved stars analyzed in this study, and their alignment with the PARSEC mass tracks, we concluded that these stars reside within the mass range $0.8 < M/M_{\odot} < 3$, corresponding to spectral types K3 and B8.5, respectively (see Z. Eker et al. 2015, 2018, 2020, 2024).

In the literature, the relations between the spectral types of stars and their scale height have been studied by many researchers (see G. Gilmore & N. Reid 1983; M. R. S. Hawkins 1988; N. Pirzkal et al. 2005; D. L. Kong & Z. Zhu 2008; B. W. Holwerda et al. 2014). These studies have shown that the thin-disk scale heights increase from 100 pc to 400 pc as it moves from O spectral type main-sequence stars to M spectral type stars. Considering that the scale heights of the evolved stars analyzed in this study range between 200 and 600 pc (see Figure A1), it is seen that the values given for stars of spectral type F and K were in agreement. This finding, together with the duration of their stay in the main sequence and the scale heights in the literature, explains the reason for the small-scale heights

of bright absolute magnitude stars and also the large-scale heights of faint absolute magnitude stars.

In this study, we utilized the high-precision photometric and astrometric data from the Gaia satellite to investigate the stellar number density and scale heights of the thin-disk population in the solar neighborhood across various Galactic coordinates and absolute magnitude intervals. Our analysis reveals that the thin-disk space densities align well with previously reported values for a 100 pc space volume. In contrast, the scale heights of evolved stars across different star fields vary substantially, ranging from 200 to 600 pc, increasing from bright absolute magnitudes ($-1 < M_G$ (mag) ≤ 0) to faint ones ($3 < M_G$ (mag) ≤ 4). This large variation in scale heights for evolved thin-disk stars over a limited range of absolute magnitudes likely reflects the evolutionary effects of stars with different masses in the solar neighborhood. Specifically, the alignment of scale heights for bright absolute magnitudes with those of early-type main-sequence stars, supported by mass track data, underscores that evolved stars exhibit varied scale heights based on their evolutionary stages. Additionally, our study confirms that Galaxy model parameters, when derived from Gaia data, vary with Galactic coordinates, object luminosities, and space volumes (e.g., S. Bilir et al. 2006a; 2006b, 2006c; S. Ak et al. 2007a; A. Cabrera-Lavers et al. 2007; S. Karaali et al. 2007; E. Yaz & S. Karaali 2010; E. Yaz Gökçe et al. 2015). The results obtained in this study using evolved stars suggest that the Galaxy model parameters should be evaluated in terms of Galactic coordinates and the absolute magnitudes of the stars.

Acknowledgments

We sincerely thank the referee for their insightful and constructive suggestions, which have significantly contributed to improving the quality and clarity of the manuscript. The authors express their gratitude to Prof. Dr. Salih Karaali for the valuable insights and inspiration that contributed to the development of this paper. We would like to thank Hikmet Çakmak for his contribution to the codes used in the analyses. This research has made use of NASA's Astrophysics Data System Bibliographic Services. Gaia,⁶ processed by the Gaia Data Processing and Analysis Consortium (DPAC).⁷ Funding for DPAC has been provided by national institutions, in particular, the institutions participating in the Gaia Multilateral Agreement.

Software: python (G. Van Rossum & F. L. Drake 2009), astropy (Astropy Collaboration et al. 2013, 2018, 2022), numpy (R. C. Harris et al. 2020), matplotlib (J. D. Hunter 2007), mwddust (J. Bovy et al. 2016a).

Appendix Additional Figures and Tables

⁶ <https://www.cosmos.esa.int/gaia>

⁷ <https://www.cosmos.esa.int/web/gaia/dpac/consortium>

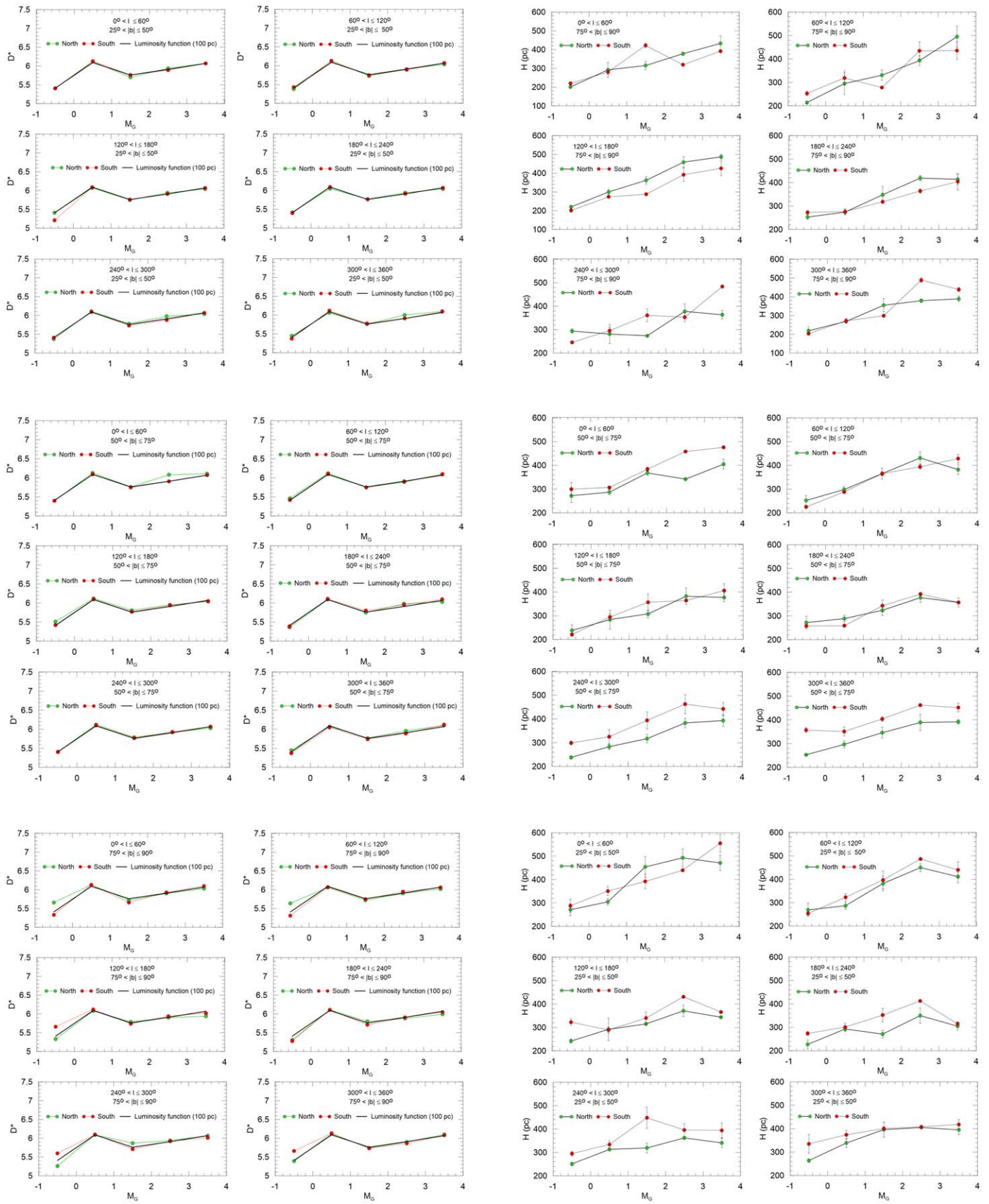


Figure A1. Space densities (left-hand panels) and scale heights (right-hand panels) estimated for different five absolute magnitude intervals of star fields within the Galactic latitude intervals in the 36-star fields. Green and red solid lines represent star fields in the north and south Galactic hemispheres, respectively.

Table A1
Galaxy Model Parameters Estimated for Five Different Absolute Magnitude Intervals in the 36-star Fields

$0^\circ < l \leq 60^\circ, 25^\circ < b \leq 50^\circ, \text{Field \#01}$					$60^\circ < l \leq 120^\circ, 25^\circ < b \leq 50^\circ, \text{Field \#02}$				
$M_1 - M_2$	N	D^*	H (pc)	$\chi^2_{\min}(10^{-7})$	$M_1 - M_2$	N	D^*	H (pc)	$\chi^2_{\min}(10^{-7})$
(-1, 0]	628	5.41 ± 0.04	271 ± 25	1.79	(-1, 0]	563	5.38 ± 0.04	269 ± 29	3.05
(0, 1]	3764	6.12 ± 0.01	305 ± 13	1.70	(0, 1]	3539	6.13 ± 0.02	287 ± 15	3.30
(1, 2]	2208	5.70 ± 0.08	454 ± 45	10.07	(1, 2]	1996	5.73 ± 0.02	382 ± 31	7.75
(2, 3]	4179	5.94 ± 0.02	493 ± 38	7.75	(2, 3]	3612	5.91 ± 0.01	450 ± 17	0.33
(3, 4]	5453	6.07 ± 0.02	471 ± 33	2.96	(3, 4]	4468	6.04 ± 0.02	411 ± 26	2.47
$120^\circ < l \leq 180^\circ, 25^\circ < b \leq 50^\circ, \text{Field \#03}$					$180^\circ < l \leq 240^\circ, 25^\circ < b \leq 50^\circ, \text{Field \#04}$				
$M_1 - M_2$	N	D^*	H (pc)	$\chi^2_{\min}(10^{-7})$	$M_1 - M_2$	N	D^*	H (pc)	$\chi^2_{\min}(10^{-7})$
(-1, 0]	521	5.41 ± 0.01	242 ± 8	0.93	(-1, 0]	489	5.42 ± 0.04	277 ± 19	6.63
(0, 1]	3078	6.07 ± 0.06	292 ± 48	29.00	(0, 1]	3014	6.05 ± 0.01	293 ± 12	2.53
(1, 2]	1690	5.75 ± 0.01	315 ± 4	10.37	(1, 2]	1445	5.77 ± 0.03	271 ± 17	2.50
(2, 3]	3162	5.94 ± 0.02	371 ± 24	2.49	(2, 3]	2958	5.94 ± 0.06	350 ± 33	11.70
(3, 4]	3666	6.04 ± 0.01	344 ± 3	0.60	(3, 4]	3180	6.04 ± 0.02	305 ± 17	8.21
$240^\circ < l \leq 300^\circ, 25^\circ < b \leq 50^\circ, \text{Field \#05}$					$300^\circ < l \leq 360^\circ, 25^\circ < b \leq 50^\circ, \text{Field \#06}$				
$M_1 - M_2$	N	D^*	H (pc)	$\chi^2_{\min}(10^{-7})$	$M_1 - M_2$	N	D^*	H (pc)	$\chi^2_{\min}(10^{-7})$
(-1, 0]	500	5.37 ± 0.01	251 ± 7	0.41	(-1, 0]	578	5.45 ± 0.01	264 ± 7	0.82
(0, 1]	3793	6.11 ± 0.01	313 ± 2	0.81	(0, 1]	3715	6.06 ± 0.02	339 ± 19	4.11
(1, 2]	1803	5.78 ± 0.02	319 ± 21	3.18	(1, 2]	2213	5.76 ± 0.02	396 ± 32	8.05
(2, 3]	3352	5.98 ± 0.01	362 ± 3	0.42	(2, 3]	4015	6.00 ± 0.01	405 ± 1	0.09
(3, 4]	3641	6.04 ± 0.02	341 ± 20	1.31	(3, 4]	4939	6.10 ± 0.01	395 ± 20	1.59
$0^\circ < l \leq 60^\circ, 50^\circ < b \leq 75^\circ, \text{Field \#07}$					$60^\circ < l \leq 120^\circ, 50^\circ < b \leq 75^\circ, \text{Field \#08}$				
$M_1 - M_2$	N	D^*	H (pc)	$\chi^2_{\min}(10^{-7})$	$M_1 - M_2$	N	D^*	H (pc)	$\chi^2_{\min}(10^{-7})$
(-1, 0]	184	5.40 ± 0.05	272 ± 28	3.48	(-1, 0]	187	5.46 ± 0.04	252 ± 21	7.96
(0, 1]	1124	6.13 ± 0.02	287 ± 11	6.44	(0, 1]	1170	6.12 ± 0.02	298 ± 13	4.29
(1, 2]	726	5.76 ± 0.01	368 ± 9	0.72	(1, 2]	691	5.75 ± 0.03	365 ± 23	9.71
(2, 3]	1357	6.08 ± 0.01	342 ± 2	0.61	(2, 3]	1231	5.89 ± 0.02	431 ± 26	2.27
(3, 4]	1905	6.11 ± 0.02	405 ± 21	3.29	(3, 4]	1715	6.10 ± 0.02	382 ± 21	6.17
$120^\circ < l \leq 180^\circ, 50^\circ < b \leq 75^\circ, \text{Field \#09}$					$180^\circ < l \leq 240^\circ, 50^\circ < b \leq 75^\circ, \text{Field \#10}$				
$M_1 - M_2$	N	D^*	H (pc)	$\chi^2_{\min}(10^{-7})$	$M_1 - M_2$	N	D^*	H (pc)	$\chi^2_{\min}(10^{-7})$
(-1, 0]	184	5.41 ± 0.13	238 ± 24	15.40	(-1, 0]	173	5.36 ± 0.05	272 ± 27	1.07
(0, 1]	1059	6.12 ± 0.06	284 ± 40	10.60	(0, 1]	1033	6.09 ± 0.02	289 ± 14	6.63
(1, 2]	609	5.81 ± 0.03	308 ± 16	6.96	(1, 2]	578	5.75 ± 0.03	324 ± 22	2.32
(2, 3]	1183	5.95 ± 0.07	382 ± 35	11.50	(2, 3]	1243	5.98 ± 0.02	377 ± 20	9.16
(3, 4]	1445	6.04 ± 0.02	377 ± 17	2.21	(3, 4]	1307	6.03 ± 0.02	357 ± 19	9.50
$240^\circ < l \leq 300^\circ, 50^\circ < b \leq 75^\circ, \text{Field \#11}$					$300^\circ < l \leq 360^\circ, 50^\circ < b \leq 75^\circ, \text{Field \#12}$				
$M_1 - M_2$	N	D^*	H (pc)	$\chi^2_{\min}(10^{-7})$	$M_1 - M_2$	N	D^*	H (pc)	$\chi^2_{\min}(10^{-7})$
(-1, 0]	144	5.41 ± 0.02	238 ± 7	0.29	(-1, 0]	179	5.45 ± 0.01	253 ± 1	0.02
(0, 1]	1055	6.12 ± 0.02	283 ± 11	1.39	(0, 1]	1021	6.07 ± 0.02	297 ± 15	1.62
(1, 2]	602	5.79 ± 0.03	317 ± 18	1.09	(1, 2]	646	5.77 ± 0.03	346 ± 23	8.09
(2, 3]	1112	5.92 ± 0.02	383 ± 20	1.08	(2, 3]	1235	5.96 ± 0.07	389 ± 34	15.30
(3, 4]	1505	6.03 ± 0.02	393 ± 24	4.20	(3, 4]	1748	6.10 ± 0.01	392 ± 9	0.97
$0^\circ < l \leq 60^\circ, 75^\circ < b \leq 90^\circ, \text{Field \#13}$					$60^\circ < l \leq 120^\circ, 75^\circ < b \leq 90^\circ, \text{Field \#14}$				
$M_1 - M_2$	N	D^*	H (pc)	$\chi^2_{\min}(10^{-7})$	$M_1 - M_2$	N	D^*	H (pc)	$\chi^2_{\min}(10^{-7})$
(-1, 0]	22	5.66 ± 0.02	201 ± 5	0.17	(-1, 0]	25	5.64 ± 0.02	214 ± 5	0.35
(0, 1]	157	6.13 ± 0.06	292 ± 39	38.00	(0, 1]	139	6.06 ± 0.07	295 ± 47	12.90
(1, 2]	70	5.72 ± 0.03	315 ± 22	1.44	(1, 2]	79	5.72 ± 0.03	331 ± 22	1.85
(2, 3]	150	5.90 ± 0.01	378 ± 8	0.51	(2, 3]	159	5.90 ± 0.02	393 ± 21	1.01
(3, 4]	252	6.03 ± 0.06	433 ± 40	84.9	(3, 4]	282	6.02 ± 0.07	495 ± 45	71.90
$120^\circ < l \leq 180^\circ, 75^\circ < b \leq 90^\circ, \text{Field \#15}$					$180^\circ < l \leq 240^\circ, 75^\circ < b \leq 90^\circ, \text{Field \#16}$				
$M_1 - M_2$	N	D^*	H (pc)	$\chi^2_{\min}(10^{-7})$	$M_1 - M_2$	N	D^*	H (pc)	$\chi^2_{\min}(10^{-7})$

Table A1
(Continued)

$0^\circ < l \leq 60^\circ, 25^\circ < b \leq 50^\circ$, Field #01					$60^\circ < l \leq 120^\circ, 25^\circ < b \leq 50^\circ$, Field #02				
$M_1 - M_2$	N	D^*	H (pc)	$\chi^2_{\min}(10^{-7})$	$M_1 - M_2$	N	D^*	H (pc)	$\chi^2_{\min}(10^{-7})$
(-1, 0]	11	5.33 ± 0.02	220 ± 7	0.35	(-1, 0]	17	5.31 ± 0.02	253 ± 10	0.63
(0, 1]	150	6.08 ± 0.02	300 ± 14	8.28	(0, 1]	132	6.11 ± 0.02	274 ± 11	1.22
(1, 2]	109	5.79 ± 0.03	362 ± 20	5.20	(1, 2]	98	5.80 ± 0.09	348 ± 35	49.60
(2, 3]	197	5.90 ± 0.02	459 ± 29	9.76	(2, 3]	180	5.88 ± 0.01	419 ± 11	0.13
(3, 4]	240	5.94 ± 0.01	487 ± 13	0.18	(3, 4]	213	5.99 ± 0.02	414 ± 22	8.95
$240^\circ < l \leq 300^\circ, 75^\circ < b \leq 90^\circ$, Field #17					$300^\circ < l \leq 360^\circ, 75^\circ < b \leq 90^\circ$, Field #18				
$M_1 - M_2$	N	D^*	H (pc)	$\chi^2_{\min}(10^{-7})$	$M_1 - M_2$	N	D^*	H (pc)	$\chi^2_{\min}(10^{-7})$
(-1, 0]	22	5.26 ± 0.01	294 ± 9	0.40	(-1, 0]	13	5.39 ± 0.20	219 ± 22	17.40
(0, 1]	132	6.09 ± 0.07	281 ± 41	31.20	(0, 1]	137	6.12 ± 0.02	269 ± 10	3.65
(1, 2]	75	5.87 ± 0.01	274 ± 2	0.10	(1, 2]	89	5.74 ± 0.10	355 ± 35	17.30
(2, 3]	160	5.94 ± 0.08	378 ± 32	17.3	(2, 3]	151	5.90 ± 0.01	379 ± 9	0.77
(3, 4]	205	6.07 ± 0.02	363 ± 18	5.10	(3, 4]	247	6.10 ± 0.02	389 ± 15	3.30
$0^\circ < l \leq 60^\circ, -50^\circ \leq b < -25^\circ$, Field #19					$60^\circ < l \leq 120^\circ, -50^\circ \leq b < -25^\circ$, Field #20				
$M_1 - M_2$	N	D^*	H (pc)	$\chi^2_{\min}(10^{-7})$	$M_1 - M_2$	N	D^*	H (pc)	$\chi^2_{\min}(10^{-7})$
(-1, 0]	662	5.40 ± 0.04	288 ± 28	2.24	(-1, 0]	596	5.43 ± 0.01	254 ± 8	0.76
(0, 1]	4558	6.13 ± 0.02	351 ± 19	2.61	(0, 1]	4035	6.12 ± 0.02	323 ± 16	8.72
(1, 2]	2175	5.76 ± 0.02	392 ± 31	9.69	(1, 2]	2148	5.75 ± 0.08	397 ± 38	11.90
(2, 3]	3390	5.89 ± 0.01	440 ± 5	0.29	(2, 3]	3730	5.89 ± 0.01	487 ± 5	0.56
(3, 4]	6402	6.07 ± 0.01	555 ± 38	1.92	(3, 4]	5212	6.07 ± 0.05	440 ± 35	13.30
$120^\circ < l \leq 180^\circ, -50^\circ \leq b < -25^\circ$, Field #21					$180^\circ < l \leq 240^\circ, -50^\circ \leq b < -25^\circ$, Field #22				
$M_1 - M_2$	N	D^*	H (pc)	$\chi^2_{\min}(10^{-7})$	$M_1 - M_2$	N	D^*	H (pc)	$\chi^2_{\min}(10^{-7})$
(-1, 0]	495	5.31 ± 0.01	323 ± 14	0.83	(-1, 0]	610	5.40 ± 0.01	274 ± 8	0.11
(0, 1]	3265	6.09 ± 0.02	289 ± 12	1.95	(0, 1]	3438	6.09 ± 0.02	301 ± 16	1.33
(1, 2]	1839	5.76 ± 0.02	340 ± 26	9.77	(1, 2]	1958	5.76 ± 0.03	352 ± 29	2.57
(2, 3]	3481	5.91 ± 0.01	431 ± 4	0.13	(2, 3]	3336	5.91 ± 0.01	413 ± 4	0.25
(3, 4]	4230	6.07 ± 0.00	366 ± 3	0.39	(3, 4]	3531	6.07 ± 0.01	315 ± 9	0.58
$240^\circ < l \leq 300^\circ, -50^\circ \leq b < -25^\circ$, Field #23					$300^\circ < l \leq 360^\circ, -50^\circ \leq b < -25^\circ$, Field #24				
$M_1 - M_2$	N	D^*	H (pc)	$\chi^2_{\min}(10^{-7})$	$M_1 - M_2$	N	D^*	H (pc)	$\chi^2_{\min}(10^{-7})$
(-1, 0]	706	5.41 ± 0.01	295 ± 10	0.41	(-1, 0]	749	5.37 ± 0.04	335 ± 40	1.67
(0, 1]	3974	6.09 ± 0.01	334 ± 15	0.81	(0, 1]	4829	6.12 ± 0.01	374 ± 18	1.64
(1, 2]	2366	5.73 ± 0.02	448 ± 45	3.18	(1, 2]	2395	5.78 ± 0.01	401 ± 5	0.43
(2, 3]	2997	5.88 ± 0.02	396 ± 27	0.42	(2, 3]	3687	5.91 ± 0.01	408 ± 4	0.67
(3, 4]	4695	6.07 ± 0.05	394 ± 32	1.31	(3, 4]	6534	6.09 ± 0.01	418 ± 21	1.52
$0^\circ < l \leq 60^\circ, -75^\circ \leq b < -50^\circ$, Field #25					$60^\circ < l \leq 120^\circ, -75^\circ \leq b < -50^\circ$, Field #26				
$M_1 - M_2$	N	D^*	H (pc)	$\chi^2_{\min}(10^{-7})$	$M_1 - M_2$	N	D^*	H (pc)	$\chi^2_{\min}(10^{-7})$
(-1, 0]	223	5.40 ± 0.05	300 ± 27	1.30	(-1, 0]	130	5.42 ± 0.02	225 ± 6	1.67
(0, 1]	1144	6.09 ± 0.01	307 ± 5	0.76	(0, 1]	1034	6.10 ± 0.01	288 ± 2	0.66
(1, 2]	766	5.75 ± 0.01	384 ± 8	0.36	(1, 2]	700	5.75 ± 0.01	365 ± 9	0.31
(2, 3]	1411	5.91 ± 0.01	458 ± 4	0.66	(2, 3]	1154	5.91 ± 0.01	394 ± 10	0.16
(3, 4]	2155	6.07 ± 0.02	476 ± 3	0.95	(3, 4]	1954	6.09 ± 0.01	428 ± 18	1.39
$120^\circ < l \leq 180^\circ, -75^\circ \leq b < -50^\circ$, Field #27					$180^\circ < l \leq 240^\circ, -75^\circ \leq b < -50^\circ$, Field #28				
$M_1 - M_2$	N	D^*	H (pc)	$\chi^2_{\min}(10^{-7})$	$M_1 - M_2$	N	D^*	H (pc)	$\chi^2_{\min}(10^{-7})$
(-1, 0]	125	5.42 ± 0.02	221 ± 6	0.69	(-1, 0]	159	5.39 ± 0.01	258 ± 7	0.13
(0, 1]	1083	6.10 ± 0.02	295 ± 14	1.78	(0, 1]	867	6.11 ± 0.01	259 ± 2	0.32
(1, 2]	649	5.77 ± 0.01	357 ± 35	30.50	(1, 2]	698	5.80 ± 0.03	343 ± 24	6.08
(2, 3]	1083	5.94 ± 0.01	364 ± 3	0.51	(2, 3]	1243	5.95 ± 0.01	392 ± 3	0.63
(3, 4]	1611	6.05 ± 0.06	406 ± 29	15.10	(3, 4]	1517	6.10 ± 0.01	357 ± 2	0.89
$240^\circ < l \leq 300^\circ, -75^\circ \leq b < -50^\circ$, Field #29					$300^\circ < l \leq 360^\circ, -75^\circ \leq b < -50^\circ$, Field #30				
$M_1 - M_2$	N	D^*	H (pc)	$\chi^2_{\min}(10^{-7})$	$M_1 - M_2$	N	D^*	H (pc)	$\chi^2_{\min}(10^{-7})$

Table A1
(Continued)

$0^\circ < l \leq 60^\circ, 25^\circ < b \leq 50^\circ$, Field #01					$60^\circ < l \leq 120^\circ, 25^\circ < b \leq 50^\circ$, Field #02				
$M_1 - M_2$	N	D^*	H (pc)	$\chi^2_{\min}(10^{-7})$	$M_1 - M_2$	N	D^*	H (pc)	$\chi^2_{\min}(10^{-7})$
(-1, 0]	222	5.40 ± 0.01	299 ± 8	0.52	(-1, 0]	286	5.37 ± 0.01	357 ± 11	0.02
(0, 1]	1249	6.10 ± 0.07	325 ± 30	1.47	(0, 1]	1300	6.05 ± 0.02	351 ± 19	1.62
(1, 2]	792	5.77 ± 0.09	394 ± 36	1.37	(1, 2]	812	5.74 ± 0.01	404 ± 9	8.09
(2, 3]	1449	5.93 ± 0.07	462 ± 40	14.90	(2, 3]	1362	5.89 ± 0.01	462 ± 4	15.30
(3, 4]	2008	6.07 ± 0.02	442 ± 27	1.03	(3, 4]	2270	6.12 ± 0.01	452 ± 18	0.97
$0^\circ < l \leq 60^\circ, -90^\circ \leq b < -75^\circ$, Field #31					$60^\circ < l \leq 120^\circ, -90^\circ \leq b < -75^\circ$, Field #32				
$M_1 - M_2$	N	D^*	H (pc)	$\chi^2_{\min}(10^{-7})$	$M_1 - M_2$	N	D^*	H (pc)	$\chi^2_{\min}(10^{-7})$
(-1, 0]	13	5.33 ± 0.02	220 ± 7	0.35	(-1, 0]	17	5.31 ± 0.02	253 ± 10	0.63
(0, 1]	141	6.13 ± 0.02	280 ± 13	4.99	(0, 1]	155	6.07 ± 0.07	319 ± 30	63.40
(1, 2]	111	5.66 ± 0.01	422 ± 12	0.17	(1, 2]	58	5.75 ± 0.01	278 ± 2	0.40
(2, 3]	118	5.93 ± 0.01	319 ± 5	0.42	(2, 3]	196	5.95 ± 0.08	435 ± 38	53.30
(3, 4]	263	6.10 ± 0.01	392 ± 8	0.66	(3, 4]	262	6.06 ± 0.06	435 ± 25	21.00
$120^\circ < l \leq 180^\circ, -90^\circ \leq b < -75^\circ$, Field #33					$180^\circ < l \leq 240^\circ, -90^\circ \leq b < -75^\circ$, Field #34				
$M_1 - M_2$	N	D^*	H (pc)	$\chi^2_{\min}(10^{-7})$	$M_1 - M_2$	N	D^*	H (pc)	$\chi^2_{\min}(10^{-7})$
(-1, 0]	22	5.66 ± 0.02	201 ± 5	0.17	(-1, 0]	21	5.28 ± 0.02	273 ± 8	0.19
(0, 1]	133	6.12 ± 0.01	274 ± 2	0.75	(0, 1]	134	6.11 ± 0.02	276 ± 12	1.68
(1, 2]	78	5.74 ± 0.01	288 ± 6	0.25	(1, 2]	71	5.71 ± 0.01	318 ± 7	0.20
(2, 3]	172	5.94 ± 0.07	392 ± 36	70.00	(2, 3]	144	5.91 ± 0.01	364 ± 9	0.17
(3, 4]	239	6.02 ± 0.01	426 ± 10	59.20	(3, 4]	230	6.05 ± 0.06	404 ± 35	13.30
$240^\circ < l \leq 300^\circ, -90^\circ \leq b < -75^\circ$, Field #35					$300^\circ < l \leq 360^\circ, -90^\circ \leq b < -75^\circ$, Field #36				
$M_1 - M_2$	N	D^*	H (pc)	$\chi^2_{\min}(10^{-7})$	$M_1 - M_2$	N	D^*	H (pc)	$\chi^2_{\min}(10^{-7})$
(-1, 0]	32	5.60 ± 0.01	246 ± 6	0.84	(-1, 0]	23	5.66 ± 0.01	204 ± 5	0.17
(0, 1]	150	6.10 ± 0.02	296 ± 14	1.40	(0, 1]	133	6.13 ± 0.02	272 ± 12	1.95
(1, 2]	88	5.71 ± 0.03	361 ± 27	2.47	(1, 2]	75	5.73 ± 0.01	299 ± 5	0.23
(2, 3]	138	5.92 ± 0.02	353 ± 19	1.16	(2, 3]	226	5.86 ± 0.01	489 ± 13	0.20
(3, 4]	290	6.01 ± 0.01	484 ± 4	0.24	(3, 4]	288	6.08 ± 0.01	439 ± 11	0.72

ORCID iDs

Sedanur İyisan <https://orcid.org/0009-0002-2272-8898>
 Selçuk Bilir <https://orcid.org/0000-0003-3510-1509>
 Özgecan Önal Taş <https://orcid.org/0000-0003-0864-1921>
 Olcay Plevne <https://orcid.org/0000-0002-0435-4493>

References

- Ak, S., Bilir, S., Karaali, S., & Buser, R. 2007a, *AN*, **328**, 169
 Ak, S., Bilir, S., Karaali, S., Buser, R., & Cabrera-Lavers, A. 2007b, *NewA*, **12**, 605
 Astropy Collaboration, Price-Whelan, A. M., Lim, P. L., et al. 2022, *ApJ*, **935**, 167
 Astropy Collaboration, Price-Whelan, A. M., Sipőcz, B. M., et al. 2018, *AJ*, **156**, 123
 Astropy Collaboration, Robitaille, T. P., Tollerud, E. J., et al. 2013, *A&A*, **558**, A33
 Bahcall, J. N., & Soneira, R. M. 1980, *ApJS*, **44**, 73
 Bilir, S., Cabrera-Lavers, A., Karaali, S., et al. 2008a, *PASA*, **25**, 69
 Bilir, S., Karaali, S., Ak, S., et al. 2009, *MNRAS*, **396**, 1589
 Bilir, S., Karaali, S., Ak, S., et al. 2008b, *MNRAS*, **390**, 1569
 Bilir, S., Karaali, S., Ak, S., Yaz, E., & Hamzaoglu, E. 2006a, *NewA*, **12**, 234
 Bilir, S., Karaali, S., & Gilmore, G. 2006b, *MNRAS*, **366**, 1295
 Bilir, S., Karaali, S., Güver, T., Karataş, Y., & Ak, S. G. 2006c, *AN*, **327**, 72
 Bilir, S., Karaali, S., & Tunçel, S. 2005, *AN*, **326**, 321
 Binney, J., & Merrifield, M. 1998, *Galactic Astronomy* (Princeton, NJ: Princeton Univ. Press)
 Bovy, J., Rix, H.-W., Green, G. M., Schlafly, E. F., & Finkbeiner, D. P. 2016a, *ApJ*, **818**, 130
 Bovy, J., Rix, H.-W., Schlafly, E. F., et al. 2016b, *ApJ*, **823**, 30
 Bressan, A., Marigo, P., Girardi, L., et al. 2012, *MNRAS*, **427**, 127
 Buser, R., Rong, J., & Karaali, S. 1998, *A&A*, **331**, 934
 Buser, R., Rong, J., & Karaali, S. 1999, *A&A*, **348**, 98
 Cabrera-Lavers, A., Bilir, S., Ak, S., Yaz, E., & López-Corredoira, M. 2007, *A&A*, **464**, 565
 Canbay, R., Bilir, S., Özdönmez, A., & Ak, T. 2023, *AJ*, **165**, 163
 Cardelli, J. A., Clayton, G. C., & Mathis, J. S. 1989, *ApJ*, **345**, 245
 Castro-Ginard, A., Penoyre, Z., Casey, A. R., et al. 2024, *A&A*, **688**, A1
 Chen, B., Stoughton, C., Smith, J. A., et al. 2001, *ApJ*, **553**, 184
 Chen, Y., Bressan, A., Girardi, L., et al. 2015, *MNRAS*, **452**, 1068
 Chrobáková, Ž., Nagy, R., & López-Corredoira, M. 2020, *A&A*, **637**, A96
 Cohen, M. 1995, *ApJ*, **444**, 874
 Du, C., Zhou, X., Ma, J., et al. 2003, *A&A*, **407**, 541
 Eker, Z., Bakış, V., Bilir, S., et al. 2018, *MNRAS*, **479**, 5491
 Eker, Z., Soyduğan, F., & Bilir, S. 2024, *PARep*, **2**, 41
 Eker, Z., Soyduğan, F., Bilir, S., et al. 2020, *MNRAS*, **496**, 3887
 Eker, Z., Soyduğan, F., Soyduğan, E., et al. 2015, *AJ*, **149**, 131
 Fenkart, R., & Karaali, S. 1987, *A&AS*, **69**, 33
 Gaia Collaboration, Babusiaux, C., van Leeuwen, F., et al. 2018, *A&A*, **616**, A10
 Gaia Collaboration, Brown, A. G. A., Vallenari, A., et al. 2021a, *A&A*, **649**, A1
 Gaia Collaboration, Prusti, T., de Bruijne, J., H., J., et al. 2016, *A&A*, **595**, A1
 Gaia Collaboration, Smart, R. L., Sarro, L. M., et al. 2021b, *A&A*, **649**, A6
 Gaia Collaboration, Vallenari, A., Brown, A. G. A., et al. 2023, *A&A*, **674**, A1
 Gilmore, G., & Reid, N. 1983, *MNRAS*, **202**, 1025
 Gokmen, S., Eker, Z., Yontan, T., et al. 2023, *AJ*, **166**, 263

- Hall, P. B., Osmer, P. S., Green, R. F., Porter, A. C., & Warren, S. J. 1996, *ApJS*, **104**, 185
- Hammersley, P. L., Garzon, F., Mahoney, T., & Calbet, X. 1995, *MNRAS*, **273**, 206
- Harris, R. C., Millman, K. J., van der Walt, S. J., et al. 2020, *Natur*, **585**, 357
- Hawkins, M. R. S. 1988, *MNRAS*, **234**, 533
- Holwerda, B. W., Trenti, M., Clarkson, W., et al. 2014, *ApJ*, **788**, 77
- Hunter, J. D. 2007, *CSE*, **9**, 90
- Jurić, M., Ivezić, Ž., Brooks, A., et al. 2008, *ApJ*, **673**, 864
- Karaali, S., Ak, S. G., Bilir, S., Karataş, Y., & Gilmore, G. 2003, *MNRAS*, **343**, 1013
- Karaali, S., Bilir, S., & Hamzaoğlu, E. 2004, *MNRAS*, **355**, 307
- Karaali, S., Bilir, S., & Tunçel, Ş. 2005, *PASA*, **22**, 24
- Karaali, S., Bilir, S., Yaz, E., Hamzaoğlu, E., & Buser, R. 2007, *PASA*, **24**, 208
- Karaali, S., Hamzaoğlu, E., & Bilir, S. 2009, *Ap&SS*, **324**, 23
- Kong, D. L., & Zhu, Z. 2008, *AcASn*, **49**, 224
- Lindgren, L., Bastian, U., Biermann, M., et al. 2021, *A&A*, **649**, A4
- Majewski, S. R. 1993, *ARA&A*, **31**, 575
- Marshall, D. J., Robin, A. C., Reylé, C., Schultheis, M., & Picaud, S. 2006, *A&A*, **453**, 635
- Ojha, D. K., Bienayme, O., Robin, A. C., Creze, M., & Mohan, V. 1996, *A&A*, **311**, 456
- Peiris, H. V. 2000, *ApJ*, **544**, 811
- Pirzkal, N., Sahu, K. C., Burgasser, A., et al. 2005, *ApJ*, **622**, 319
- Schlafly, E. F., & Finkbeiner, D. P. 2011, *ApJ*, **737**, 103
- Siegel, M. H., Majewski, S. R., Reid, I. N., & Thompson, I. B. 2002, *ApJ*, **578**, 151
- Skrutskie, M. F., Cutri, R. M., Stiening, R., et al. 2006, *AJ*, **131**, 1163
- Tang, J., Bressan, A., Rosenfield, P., et al. 2014, *MNRAS*, **445**, 4287
- Tasdemir, S., & Yontan, T. 2023, *PARep*, **1**, 1
- Van Rossum, G., & Drake, F. L. 2009, Python 3 Reference Manual (Scotts Valley, CA: CreateSpace)
- Wang, H.-F., Liu, C., Xu, Y., Wan, J.-C., & Deng, L. 2018, *MNRAS*, **478**, 3367
- Yaz, E., & Karaali, S. 2010, *NewA*, **15**, 234
- Yaz Gökçe, E., Karaali, S., Duran, Ş, et al. 2015, *PASA*, **32**, e012
- Yontan, T., & Canbay, R. 2023, *PARep*, **1**, 65
- York, D. G., Adelman, J., Anderson, John, E. J., et al. 2000, *AJ*, **120**, 1579
- Yu, Y., Wang, H.-F., Cui, W.-Y., et al. 2021, *ApJ*, **922**, 80